nature physics

ARTICLES

https://doi.org/10.1038/s41567-021-01302-3

Topological frequency combs and nested temporal solitons

Sunil Mittal[1,2] ✉, Gregory Moille[1,3], Kartik Srinivasan[1,3], Yanne K. Chembo[2] and Mohammad Hafezi[1,2,4]

Recent advances in realizing optical frequency combs using nonlinear parametric processes in integrated photonic resonators have revolutionized on-chip optical clocks, spectroscopy and multichannel optical communications. At the same time, the introduction of topological physics in photonic systems has allowed the design of photonic devices with novel functionalities and inherent robustness against fabrication disorders. Here we use topological design principles to theoretically propose the generation of optical frequency combs and temporal dissipative Kerr solitons in a two-dimensional array of coupled ring resonators that creates a synthetic magnetic field for photons and exhibits topological edge states. We show that these topological edge states constitute a travelling-wave super-ring resonator that leads to the generation of coherent nested optical frequency combs, as well as the self-formation of nested temporal solitons and Turing rolls that are remarkably phase-locked over more than 40 rings. Moreover, we show that the topological nested solitons are robust against defects in the lattice, and a single nested soliton achieves a mode efficiency of over 50%, an order of magnitude higher than single-ring frequency combs. Our topological frequency comb works in a parameter regime that can be readily accessed using existing low-loss integrated photonic platforms like silicon nitride.

While optical frequency combs naturally emerge in mode-locked ultrafast lasers[1–3], the use of nonlinear parametric processes—particularly the Kerr effect—in integrated photonic resonators offers a much more convenient and compact route to generate optical frequency combs[4–8]. Of particular significance is the regime of coherent optical frequency combs where the intrinsic dispersion and dissipation of a photonic resonator are counterbalanced by nonlinearity-induced dispersion and parametric gain, respectively, and this double-balance leads to the self-formation of stationary temporal solutions called dissipative Kerr solitons (DKSs)[5]. DKSs have been demonstrated in a variety of single-resonator geometries, and diverse material platforms such as silica glass, silicon nitride, and so on[5,6,9]. More recently, DKSs have been explored in photonic molecules, that is, a configuration of two coupled resonators, which allows the exploration of collective coherence or self-organization of solitons as well as solitonic solutions that are inaccessible using a single resonator[10–13].

In parallel, advances in the field of topological photonics have allowed access to new paradigms that can be used to design photonic devices with novel functionalities[14–16]. On one hand, topological photonic systems use complex arrays of hundreds of coupled waveguides or ring resonators[17–19]. On the other hand, such systems exhibit remarkably simple features such as edge states, which are dictated only by the global topology and therefore are independent of local details of the system. This unique property of edge states protects them against local defects and disorders in the system, enabling the realization of robust photonic devices such as optical delay lines[17,18,20], lasers[21–24], switches[25,26], photonic crystal waveguides and cavities[27–29], fibres[30], etc. Lately, topological edge states have also been used in conjunction with nonlinear parametric processes for the efficient and tunable generation of quantum states of light via spontaneous four-wave mixing[31–33], optical frequency conversion[34,35], as well as to explore spatial solitons in coupled waveguide arrays[36–39].

Here we theoretically investigate the generation of coherent optical frequency combs and temporal DKSs in a topological photonic system consisting of a two-dimensional lattice of coupled (micro)ring resonators. We exploit the fact that the topological edge states circulate around the boundary of the lattice, and because of their unidirectionality, they constitute a travelling-wave super-ring resonator formed of multiple single-ring resonators (Fig. 1e). We show that pumping the edge state super-ring resonator with a continuous-wave (CW) laser—of optimal frequency and power—leads to the self-formation of temporal patterns, particularly Turing rolls and nested DKSs. More importantly, these temporal patterns are phase-locked across all the ring resonators on the edge of the lattice, indicating collective coherence or self-organization across more than 40 oscillators. In the regime of nested solitons, the spectral output of our device corresponds to that of a coherent nested optical frequency comb (Fig. 1f). We find that the nested solitons inherit the topological protection of a linear system and are robust against any defects in the lattice. From an application perspective, in the regime of a single nested soliton, the topological frequency comb achieves a mode efficiency of >50%, an order of magnitude higher than single-ring frequency combs[40–42] that are theoretically limited to only ~5%. Our design can be readily implemented with the existing nanofabrication technology (Supplementary Section 3), and similar topological ring resonator systems with nonlinear parametric processes have already been realized to enhance and engineer the generation of quantum states of light[31,32].

[1]Joint Quantum Institute, National Institute of Standards and Technology/University of Maryland, College Park, MD, USA. [2]Department of Electrical and Computer Engineering and IREAP, University of Maryland, College Park, MD, USA. [3]Microsystems and Nanotechnology Division, Physical Measurement Laboratory, National Institute of Standards and Technology, Gaithersburg, MD, USA. [4]Department of Physics, University of Maryland, College Park, MD, USA. ✉e-mail: mittals@umd.edu

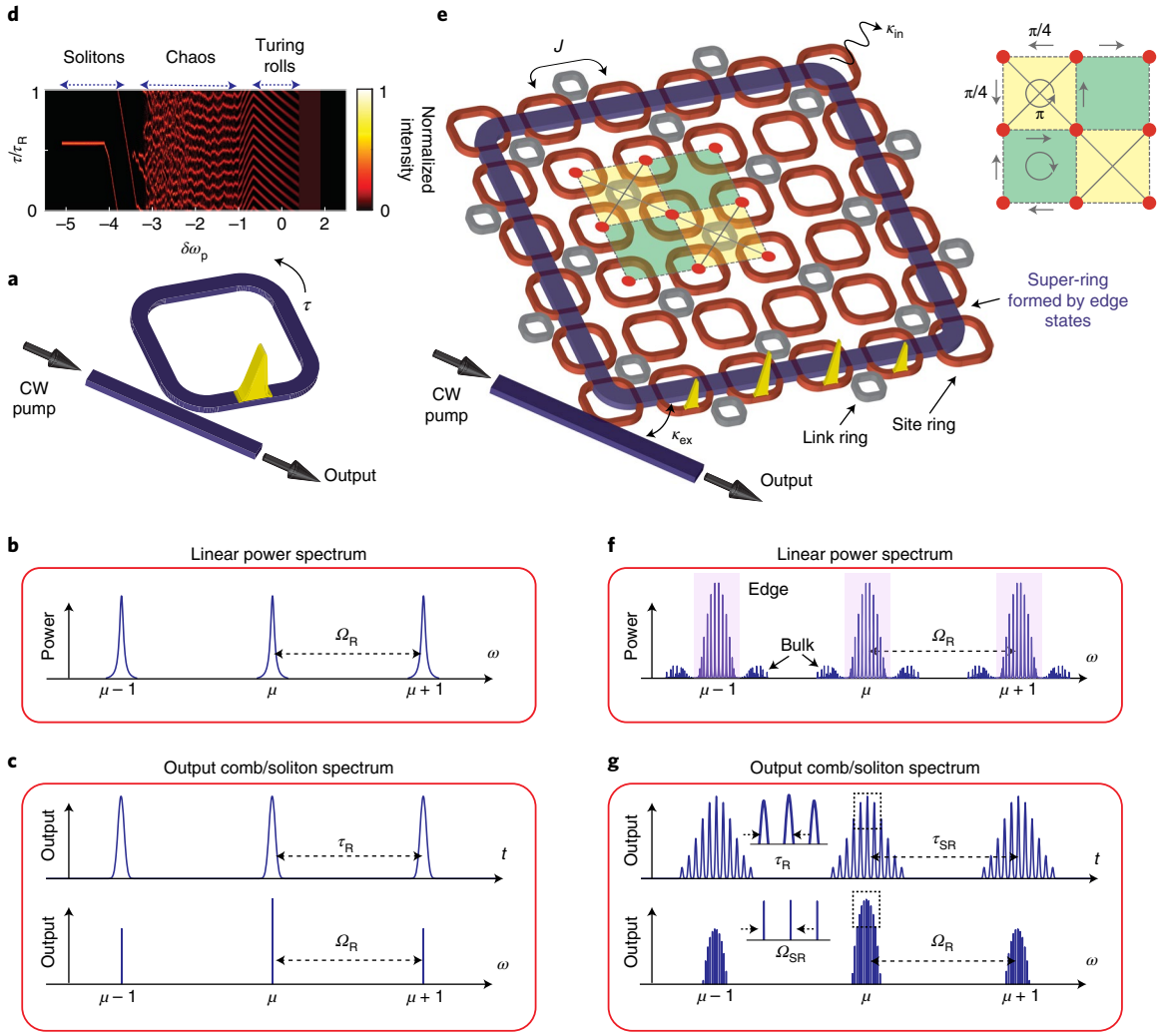

Fig. 1 | Working of the topological frequency comb. a,**b**, Schematic of a single-ring resonator (**a**) and its power spectrum in the linear regime (**b**). **c**, Temporal and spectral response at the output of the ring resonator in the regime of a single Kerr soliton. The temporal output consists of a series of pulses separated by τ_R, the round-trip time of the ring resonator. The spectral output consists of a series of narrow lines separated by FSR Ω_R. **d**, An indicative spatiotemporal intensity distribution in the ring, showing different operating regimes as a function of input pump frequency detuning $\delta\omega_p$ from cold-cavity resonance (Supplementary Fig. 3). **e**, Schematic of a two-dimensional array of ring resonators that simulates the anomalous quantum Hall model for photons and exhibits topological edge modes at its boundary. **f**, Power spectrum in the linear regime showing edge state resonances (shaded) and bulk bands. The edge states extend throughout the boundary of the lattice and constitute a super-ring resonator, with longitudinal mode separation Ω_{SR}. The transmission spectrum repeats every FSR Ω_R of the ring resonators. When pumped by a CW laser near one of the edge mode resonances, the topological super-ring can host nested solitons with indicative spatial intensity profile shown by yellow-coloured pulses. **g**, Schematic of the temporal and spectral output of the topological frequency comb in the regime of a single nested soliton. The output temporal profile consists of a series of soliton pulses separated by single-ring round-trip time τ_R (fast time), modulated by a series of super-soliton pulses separated by the round-trip time τ_{SR} (slow time) of the edge mode super-ring. The output spectral profile shows a nested comb, that is, a series (comb) of edge mode resonances (longitudinal modes of the super-ring; slow frequency) oscillating in each FSR (fast frequency) of the the single-ring resonators.

Topological system and simulation framework

Our topological system consists of a square lattice with a site-ring resonator located at each of its lattice sites (Fig. 1e)[43,44] (Supplementary Section 1). The site-ring resonators are coupled to their nearest and next-nearest neighbours, using another set of link rings, such that a non-zero local synthetic magnetic field for photons with flux π threads a half-unit cell, but the flux threading a complete unit cell is zero. Close to a given longitudinal mode resonance of the site rings, the lattice simulates a Haldane-like anomalous quantum Hall model for photons. Accordingly, its power spectrum (or the energy-momentum band structure) exhibits a topological edge band sandwiched between two bulk bands (Fig. 1f and Supplementary Section 1). The edge states propagate all along the boundary of the lattice in a single direction (set by the input port[44]) and therefore constitute a travelling-wave super-ring resonator (Fig. 1e and Supplementary Fig. 1). The multiple longitudinal modes of the super-ring—equally separated in frequency by free spectral range (FSR) Ω_{SR}—are clearly evident in the edge band of the power spectrum. Furthermore, this structure of an edge band sandwiched between two bulk bands repeats in frequency every FSR (longitudinal mode spacing Ω_R) of the individual ring resonators. Therefore, our topological system effectively involves three dimensions—two real dimensions in space and one synthetic dimension in frequency that is associated with the longitudinal modes of the ring resonators.

To generate an optical frequency comb in this lattice, we couple one ring at the edge of the lattice to an input–output waveguide, as shown in Fig. 1e. At the input port of this waveguide, we inject a CW pump laser with frequency close to one of the longitudinal mode resonances of the ring resonators (indexed by an integer $\mu = 0$). The intrinsic Kerr nonlinearity of the ring resonators leads to spontaneous four-wave mixing and subsequently stimulates the generation of photons in other longitudinal modes ($\mu \neq 0$) in the form of a frequency comb.

To simulate the generation of an optical frequency comb in the lattice, we derive the coupled driven-dissipative nonlinear Schrödinger equations, also called Lugiato–Lefever equations[6,45,46], which dictate the complete spatial, spectral and temporal evolution of site-ring fields as

$$\begin{aligned}\frac{\mathrm{d}a_{m,\mu}}{\mathrm{d}t} &= -i\left(\omega_{0,\mu} - \Omega_\mathrm{R}\,\mu - \omega_\mathrm{p}\right) a_{m,\mu} - J\sum_{\langle n\rangle} a_{n,\mu}\,\mathrm{e}^{-i\phi_{m,n}} \\ &\quad -J\sum_{\langle\langle n\rangle\rangle} a_{n,\mu} + i\gamma\,\tfrac{1}{\tau_\mathrm{R}}\int_0^{\tau_\mathrm{R}} \mathrm{d}\tau\left(|\tilde{a}_{m,\tau}|^2\tilde{a}_{m,\tau}\right)\mathrm{e}^{-i\omega_\mu\tau} \qquad (1)\\ &\quad -\left(\kappa_\mathrm{ex}\,\delta_{m,\mathrm{IO}} + \kappa_\mathrm{in}\right) a_{m,\mu} + \delta_{m,\mathrm{IO}}\,\delta_{\mu,0}\,\mathcal{E}.\end{aligned}$$

Here $a_{m,\mu}$ is the photon field for the site ring at spatial position m for a given longitudinal mode μ; J is the coupling strength between the ring resonators and is the same for both nearest-neighbour (indicated by $\langle m,n\rangle$) and next-nearest-neighbour (indicated by $\langle\langle m,n\rangle\rangle$) couplings. The hopping phase $\phi_{m,n} = \pm\frac{\pi}{4}$ for nearest-neighbour couplings and $\phi_{m,n} = 0$ for the next-nearest-neighbour couplings (Supplementary Section 1). Further, γ is the strength of the nonlinear interaction, κ_ex is the coupling rate of the input–output (IO) ring (indicated by $\delta_{m,\mathrm{IO}}$) to the input–output waveguide, and κ_in is the loss rate of the ring resonators; $\mathcal{E}$ is the normalized input pump field, which is coupled only to the IO ring, and is in the longitudinal mode $\mu = 0$ (indicated by $\delta_{\mu,0}$). Also, $\omega_{0,\mu}$ is the resonance frequency of the site-ring resonators for a longitudinal mode with index μ and includes second-order anomalous dispersion D_2 such that

$$\omega_{0,\mu} = \omega_0 + \Omega_\mathrm{R}\,\mu + \frac{D_2}{2}\,\mu^2. \qquad (2)$$

The input pump frequency is denoted by ω_p and the pumped longitudinal mode corresponds to $\mu = 0$ with resonance frequency ω_0. The coupled equations (1) have been written in a reference frame rotating at frequency $\Omega_\mathrm{R}/2\pi$ such that the FSR of the individual ring resonators is an independent parameter (equations (1) and (2)). Also, note that we have not made any assumptions regarding the spectral position, bandwidth or dispersion of the edge state resonances within a longitudinal mode μ (Supplementary Section 8).

In equation (1), the nonlinear four-wave mixing interaction between different longitudinal mode resonances is represented in the time domain τ (in $[0,\tau_\mathrm{R}]$), which corresponds to the round-trip time within a single-ring resonator[47,48]. Specifically, in a reference frame rotating at frequency $\Omega_\mathrm{R}/2\pi = 1/\tau_\mathrm{R}$, $\tilde{a}_{m,\tau}$ represents the spatiotemporal field within a ring, at lattice location m, and is related to the spectral field within the ring as

$$a_{m,\mu} = \frac{1}{\tau_\mathrm{R}}\int_0^{\tau_\mathrm{R}} \mathrm{d}\tau\,\tilde{a}_{m,\tau}\mathrm{e}^{-i\omega_{0,\mu}\tau}. \qquad (3)$$

We emphasize that the spectral and temporal dynamics of our system, as dictated by equation (1), involves two disparate frequency and time scales: (1) fast frequency associated with the longitudinal mode resonances of individual rings (indexed by μ and separated by Ω_R) and corresponding fast timescale τ in $[0,\tau_\mathrm{R}]$ that depicts the spatiotemporal field within individual rings; (2) slow frequency (ω_slow) associated with the longitudinal mode resonances of the super-ring resonator (separated by Ω_SR), that is, the frequency response close to a given longitudinal mode resonance of the individual rings and the corresponding slow time $t \approx 1/J$ that depicts the evolution of fields within the super-ring with round-trip time τ_SR. While equations (1) and (3) directly yield the fast-time and fast-frequency response, the Fourier transform of the slow-time (t) evolution of $a_{m,\mu}$ allows us to reconstruct the slow-frequency (ω_slow) spectrum of the topological comb.

For our numerical simulations, we consider a 12×12 lattice of site rings and 256 FSRs of individual rings. We use dimensionless parameters[45,46] such that the relevant frequency ($\omega_{0,\mu}$, ω_p, κ_ex, κ_in, Ω_R and D_2) and time (τ_R and t) scales are normalized by coupling strength J, and the fields ($a_{m,\mu}$) are normalized by ratio $\sqrt{J/\gamma}$ (effectively, $J = 1$ and $\gamma = 1$; Supplementary Section 2). We chose $\kappa_\mathrm{ex} = 0.050$ and $\kappa_\mathrm{in} = 0.005$ such that the individual edge state resonances in the edge band are resolved, and $D_2 = 0.00025$.

Turing rolls and collective coherence

To understand the generation of an optical frequency comb in our topological device, we first fix the (normalized) input pump field at $\mathcal{E} = 1.1$, and observe the output spectra of the generated photons across multiple FSRs (fast frequency, indexed by μ) as we tune the input pump frequency in one of the FSRs ($\mu = 0$; Fig. 2a,b). We find that the generation of the frequency comb (bright light intensity across multiple FSRs) is efficient only when the input pump frequency is close to one of the edge mode resonances. Furthermore, as we will show later, on pumping near the edge mode resonances, the bright frequency comb is generated only in the ring resonators that lie on the edge of the lattice. By contrast, when the input pump frequency is in the bulk bands, the generation of light in FSRs other than the pumped FSR is very weak and the frequency comb is inefficient. This enhanced generation of the optical frequency comb in the edge band is due to the travelling-wave super-ring resonator formed by the edge states that efficiently reinforces the optical frequency comb. The bulk states, on the other hand, do not have a well-defined direction of flow of photons in the lattice (Supplementary Fig. 1).

Having established that the topological optical frequency comb is efficient only when the input pump frequencies excite the edge modes, we now focus on pump frequencies near a single edge mode of the lattice. Figure 2c shows the total pump power $\left(\sum_{m\in\mathrm{edge}}|a_{m,\mu=0}|^2\right)$ in the super-ring resonator as a function of pump frequency detuning. To reveal the self-formation of temporal features, we plot $\sum_{m\in\mathrm{edge}}|\tilde{a}_{m,\tau}|^2$ (Fig. 2d), that is, the spatiotemporal (or fast-time τ) intensity distribution integrated over the rings on the edge of the lattice, as a function of the input pump frequency. The presence of sharp features in this plot indicates both self-formation of temporal (or equivalently, spatial) features within individual ring resonators and self-organization of these features across the rings. Randomly varying features in this plot indicate randomness in the spatial intensity distribution within the rings or a lack of coherence between the rings. This plot can be compared with the corresponding plot of a single-ring resonator frequency comb (Fig. 1d and Supplementary Fig. 3).

When the input pump frequency is at $\delta\omega_{\mathrm{p_1}} = 0.111J$ in Fig. 2d, we observe a regularly oscillating pattern along the fast-time τ axis, which indicates the formation of Turing rolls[5,6] (Supplementary Fig. 3). To confirm this, we plot the spatiotemporal intensity distribution within each ring of the lattice (Fig. 2e), that is, $|\tilde{a}_{m,\tau}|^2$, where $m = (m_x, m_y)$ indicates the location of a ring in the lattice (Supplementary Fig. 1). Indeed, all the rings on the edge of the lattice exhibit equally spaced pulses, called Turing rolls (or perfect soliton crystals)[5,6]. Also, the light intensity in the bulk of the lattice is negligible. Remarkably, we find that the phase of the

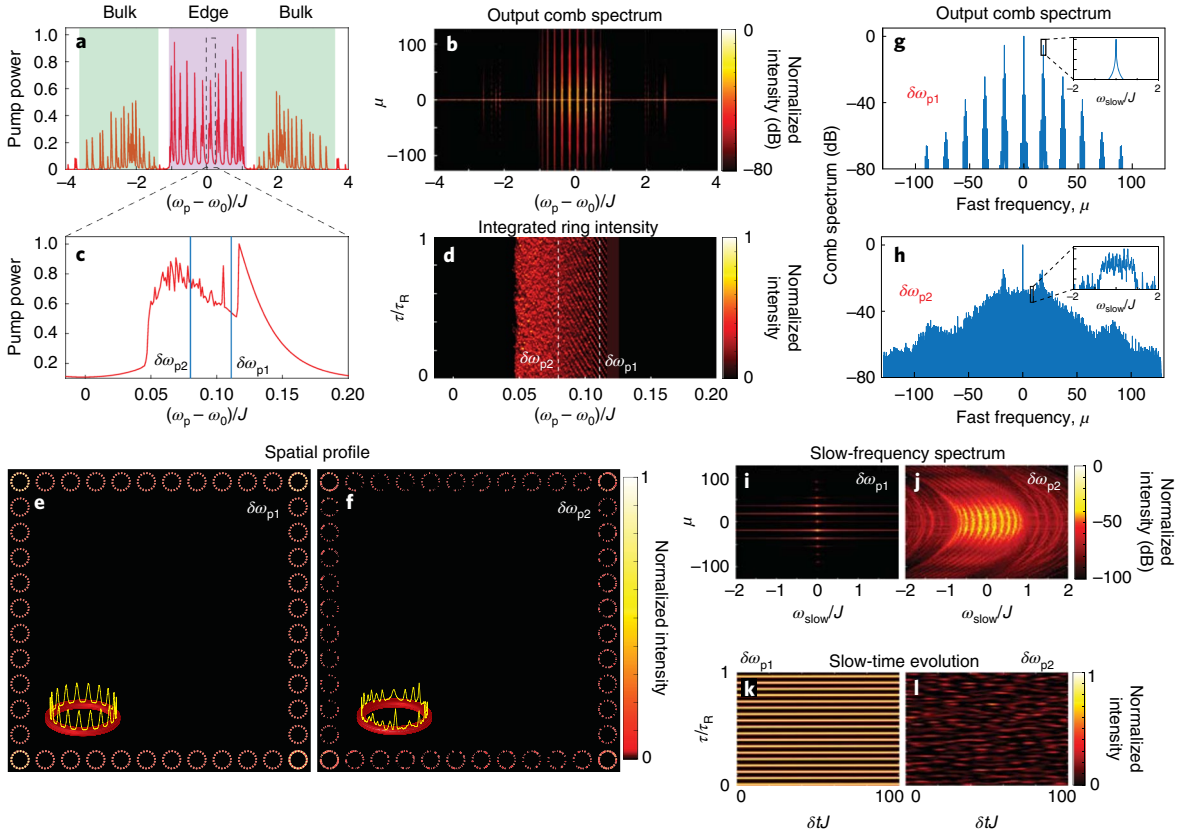

Fig. 2 | Operation of topological comb in the regimes of Turing rolls and chaos. a, Total pump power in the super-ring resonator as a function of the input pump frequency detuning $(\omega_p-\omega_0)/J$, with normalized input pump field $\varepsilon=1.1$. **b**, Spectral power of the generated frequency comb $\left(2\kappa_{ex}\left|a_{IO,\mu}\right|^2\right)$ in different FSRs (indexed by μ, the fast frequency). **c**, Total pump power in the super-ring resonator, for pump frequencies in one of the edge state resonances. **d**, Spatiotemporal (or fast-time) intensity distribution in the ring resonators, integrated over the rings on the edge of the lattice $\left(\sum_{m\in edge}|\tilde{a}_{m,\tau}|^2\right)$, as a function of pump frequency detuning. This plot can be compared with that of a single-ring resonator, as shown in Fig. 1d. We analyse two different pump frequencies, namely, $\delta\omega_{p_1}=0.111J$ and $\delta\omega_{p_2}=0.080J$, as indicated in **c** and **d**. **e**–**h**, Spatial intensity distribution in the lattice (**e**,**f**) and output comb spectra (**g**,**h**) at $\delta\omega_{p_1}$ (**e**,**g**) and $\delta\omega_{p_2}$ (**f**,**h**), in the regimes of phase-locked Turing rolls and chaos, respectively. The insets in **e** and **f** show the spatiotemporal intensity distribution in the input–output ring. The insets in **g** and **h** show the slow-frequency spectra for a given longitudinal mode μ. For plotting the comb spectra, we chose $\Omega_R=20$. **i**–**l**, Slow-frequency spectra (**i**,**j**) and slow-time temporal profiles (**k**,**l**) at the output for pump frequencies $\delta\omega_{p_1}$ and $\delta\omega_{p_2}$, respectively.

Turing rolls is locked throughout the edge of the lattice. This shows self-organization or collective spectrotemporal coherence between all the 44 rings on the edge. In fact, there exists a broad region with a bandwidth of ~$0.01J$, where we observe coherent Turing rolls. From Fig. 2c, we also see that the pump power in the super-ring smoothly varies in this region of coherent Turing rolls (Supplementary Fig. 3).

For lower pump frequencies (near $\delta\omega_{p_2}$ in Fig. 2c,d), we find a chaotic region where the pump power rapidly varies as we tune the input pump frequency. More importantly, the spatiotemporal intensity distribution within each ring, as well as the distribution across rings, is now random without any coherence whatsoever. We emphasize that the pump frequency is still in the edge band, and consequently, the comb intensity is confined to the edge of the lattice and the intensity in the bulk is negligible.

Figure 2g,h shows the output comb spectra for the two pump frequencies $\delta\omega_{p_1}$ and $\delta\omega_{p_2}$. For $\delta\omega_{p_1}$, the frequency comb spectrum predominantly consists of discrete spectral lines, separated by 18 FSRs. As in the case of a single-ring frequency comb, this number exactly corresponds to the number of Turing rolls in each ring (Fig. 2e). Furthermore, we have confirmed that the number of Turing rolls decreases as $\sqrt{\gamma/D_2}$ (refs. [6,45,48]) (Supplementary Fig. 4). At $\delta\omega_{p_2}$, that is, in the chaotic region, the discrete lines in the primary comb merge together, and there are no distinct features in the frequency spectrum.

Because $\omega_{slow}\approx J\ll\Omega_R$, the slow-frequency spectrum of the comb is not resolved in Fig. 2g,h, which shows the spectra along the fast-frequency axis (FSRs, μ). Therefore, to better visualize the slow-frequency response of the topological comb, we plot the slow-frequency spectrum within each FSR (Fig. 2i,j). Here ω_{slow} (x axis) is calculated as the detuning from the corresponding longitudinal mode resonance frequency $\omega_{0,\mu}$ and the input pump frequency, such that $\omega_{slow}=\{(\omega_\mu-\omega_{0,\mu})-(\omega_p-\omega_0)\}/J$, where ω_μ is the frequency of generated light in longitudinal mode μ.

At $\delta\omega_{p_1}$, that is, in the region of coherent Turing rolls (Fig. 2i), the slow-frequency spectrum within each bright FSR (fast frequency, μ) exhibits a single mode centred around the comb line (a cross-section of this plot is shown in Fig. 2g, inset). The oscillation of a single edge mode within each oscillating FSR is consistent with the observation of uniform spatial intensity distribution on the edge of the lattice (Fig. 2e). This can also be inferred from Fig. 2k, which shows that the fast-time (τ) intensity distribution at the output remains constant with the evolution of slow time t.

At $\delta\omega_{p_2}$, that is, in the chaotic region, we observe the oscillation of multiple modes in the edge band ($\omega_{slow}=(-1,1)J$) of each FSR.

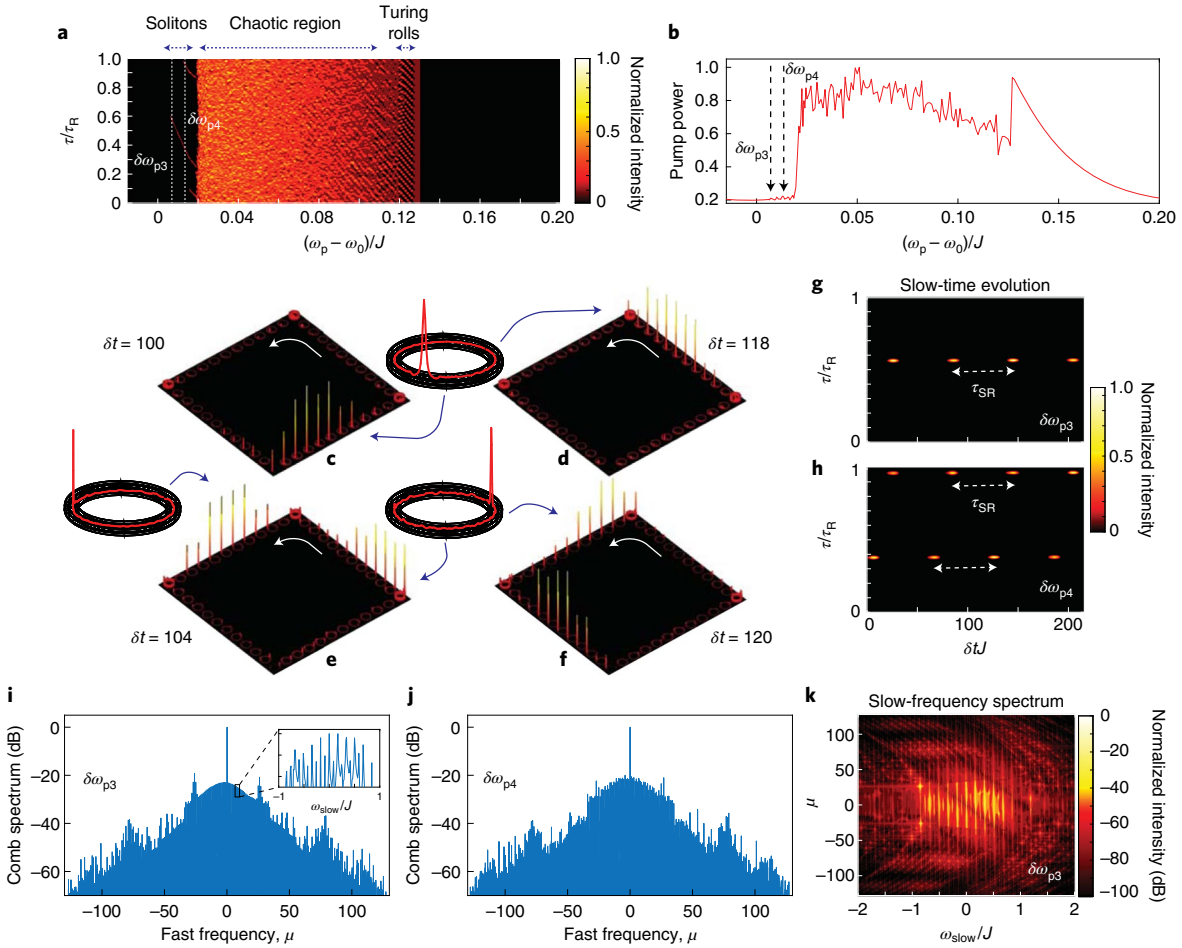

Fig. 3 | Operation of topological comb in the regime of a nested solitons. a, Spatiotemporal (or fast-time) intensity distribution integrated over edge rings. **b**, Total pump power in the super-ring resonator as a function of the input pump frequency, with input pump field $\varepsilon = 1.56$. **c**,**d**, Spatial intensity profiles in the lattice at $\delta\omega_{p_3}$, for two different slow times, $\delta t = 100$ (**c**) and $\delta t = 118$ (**d**), showing the propagation of a single nested soliton (Supplementary Video 1). The inset shows the phase (or position) of the soliton, which is the same for each ring resonator. **e**,**f**, Propagation of two nested solitons at pump frequency $\delta\omega_{p_4}$, at two different slow times $\delta t = 104$ (**e**) and $\delta t = 120$ (**f**) (also see Supplementary Video 2). The phases of the solitons in individual rings (shown in the insets) are different in the two nested solitons. **g**,**h**, Temporal profiles at the output for pump frequencies $\delta\omega_{p_3}$ (**g**) and $\delta\omega_{p_4}$ (**h**). **i**,**j**, Output comb spectra for $\delta\omega_{p_3}$ (**i**) and $\delta\omega_{p_4}$ (**j**). The inset in **i** shows the slow-frequency spectrum (for a given longitudinal mode μ) where multiple equidistant edge modes are oscillating. **k**, Slow-frequency spectrum at $\delta\omega_{p_3}$, showing the oscillation of individual edge mode resonances with an effectively linear dispersion.

This oscillation of multiple edge modes in the chaotic regime is also evident from the non-uniformity of the spatial intensity distribution in the lattice (Fig. 2f), and the dynamics of the output temporal profile (Fig. 2l) that randomly varies with slow time t. Furthermore, spectral power in the bulk modes ($\omega_{slow} < -1J$ and $\omega_{slow} > 1J$) is two orders of magnitude smaller compared with those of the edge modes. This validates the observation of negligible light intensity in the bulk of the lattice (Fig. 2f). Note that the oscillating edge modes (Fig. 2j) also show the underlying quadratic dispersion of the ring resonators in different FSRs.

Temporal Kerr super-solitons

To show the presence of nested solitons in the topological frequency comb, we increase the normalized input pump field to $\varepsilon = 1.56$. From the spatiotemporal intensity distribution in the super-ring resonator (Fig. 3a), in addition to the coherent Turing rolls and chaotic regions, we observe a new regime (0–0.02J) where the light intensity is confined to very narrow regions (thin strands) in the ring resonators. A quick comparison with the analogous spatiotemporal intensity distribution of a single-ring optical frequency comb (Fig. 1d) reveals that this region hosts solitons in the topological frequency comb. Figure 3b shows the total pump power in the super-ring resonator where—similar to a single-ring comb—we see the emergence of kinks in the region where we expect solitons.

We analyse two different pump frequencies, namely, $\delta\omega_{p_3} = 0.0070J$ and $\delta\omega_{p_4} = 0.0135J$, in this region, as indicated in Fig. 3. From the spatial intensity distribution (Fig. 3c), we see that at $\delta\omega_{p_3}$, the topological frequency comb exhibits nested solitons: the intensity distribution along the super-ring resonator (edge) of the lattice is confined to a small region of the edge in the form of a super-soliton, and the intensity distribution within each ring is also confined to a narrow region in the form of a soliton. This nested soliton then circulates along the edge of the lattice in an anticlockwise direction as slow time t evolves (Supplementary Video 1). Remarkably, the spatiotemporal phase of the solitons in individual rings of the super-soliton is locked (Fig. 3c, inset) as this nested soliton structure circulates around the edge of the lattice. This observation once again highlights the collective coherence or self-organization of multiple nonlinear ring resonators on the edge of the lattice. The corresponding temporal spectrum (Fig. 3g) at the output of the topological frequency comb then shows pulses of light that are separated by τ_{SR}, the round-trip time of the super-ring

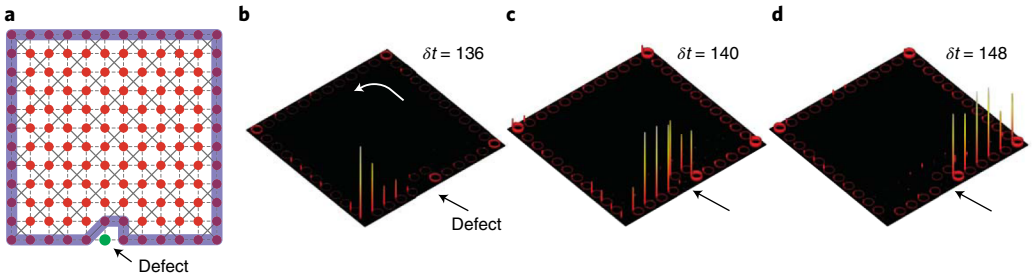

Fig. 4 | Robustness of the topological comb. a, Schematic of the lattice with a deliberately located defect on the boundary. **b**–**d**, Robust propagation of a single nested soliton around the defect, at different slow times $\delta t = 136$ (**b**), 140 (**c**) and 148 (**d**), without any loss of phase-locking or any scattering into the bulk (Supplementary Video 3).

resonator. Note that our simulations are carried out in a reference frame that is rotating at frequency $\Omega_R/2\pi$, that is, co-propagating with the solitons in individual rings. Therefore, the solitons in each ring are circulating with time period τ_R, and each super-soliton pulse (shown in Fig. 3g) is actually a burst of pulses separated by time τ_R (Fig. 1g).

At input pump frequency $\delta\omega_{p_4}$, we observe two sets of nested solitons that are simultaneously circulating along the edge of the lattice (Fig. 3e,f and Supplementary Video 2). Furthermore, while the phases of the individual ring solitons within each nested soliton are locked, the corresponding phases in the two nested solitons are not the same (Fig. 3e,f, insets). In contrast to a single nested soliton, the temporal spectrum at the output of the topological frequency comb now consists of two bursts of pulses in each round-trip time τ_{SR} of the super-ring resonator. At other pump frequencies in the super-soliton region, we can also observe three nested solitons.

Next, we discuss the frequency spectrum at the output of the topological frequency comb (Fig. 3i,j). In the case of a single nested soliton, that is, at $\delta\omega_{p_3}$, the output frequency spectrum is—in general—smooth, which indicates that it is phase-locked (except for few phase jumps; Supplementary Fig. 4). By contrast, in the case of two nested solitons, that is, at $\delta\omega_{p_4}$, the frequency spectrum shows small variations (Fig. 3j). This behaviour of the frequency spectra is similar to that observed in single-ring resonator frequency combs where the spectrum is phase-locked only when a single soliton exists in the ring[5,6,45,46].

Furthermore, by resolving the slow-frequency (ω_{slow}) response of the topological comb (Fig. 3k), we find multiple edge modes that are oscillating within each FSR (Fig. 3i, inset). More importantly, the oscillating edge modes are equally spaced within a given FSR and across FSRs, that is, the intrinsic (linear) dispersion of the longitudinal modes—of both individual ring resonators and super-ring resonator—has now been exactly cancelled by the dispersion induced by the Kerr nonlinearity. Therefore, the frequency spectrum in the regime of a single nested soliton indeed corresponds to that of a coherent nested frequency comb (Fig. 1g). The slow-frequency response also explains the emergence of kinks, as shown in Fig. 3i—these are the regions in which the dispersion curves from two different edge modes interfere and lead to phase jumps in the otherwise coherent frequency comb. This slow-frequency spectrum in the soliton regime can be compared with that of the chaotic regime (Fig. 2j and Supplementary Fig. 5), where multiple modes in the edge band are oscillating but there is no cancellation of dispersion and no phase coherence.

A figure of merit for optical frequency combs operating in the regime of a single soliton is the mode efficiency at the output of the device, that is, the fraction of power that resides in the comb lines other than the pumped mode (Supplementary Section 4). For single-ring resonator optical frequency combs, the mode efficiency in the regime of a single soliton is limited to ~5%, irrespective of the length, quality factor or material of the resonator[40–42]. This is because the pulse width of a single soliton is much smaller than the round-trip time of the resonator, which leads to a very small temporal overlap with a CW pump. In comparison, in the regime of a single nested soliton of the topological comb, we observe that 53% of the total output power (in the waveguide) is contained in the comb lines other than the pumped edge mode. This mode efficiency is an order of magnitude higher than that of single-ring resonators and is due to the fact that a single nested soliton pulse (in the super-ring) spans multiple phase-locked ring resonators, with each ring supporting its own single soliton pulse. This enhances the temporal overlap of the nested soliton pulse with the pump. We note that a single-ring comb can also achieve higher efficiency when multiple solitons are present in the ring resonator[5]. However, in this case, the phase (position along the ring) of each soliton pulse is different, and therefore, the comb spectrum is not smooth. In the case of a topological nested soliton, a single ring hosts only a single soliton, and the phase of the solitons across multiple rings is exactly the same, which leads to a smooth spectrum (Fig. 3g). We note that the theoretical limit on the conversion efficiency of the topological nested frequency comb (in the regime of a single nested soliton) could be higher for other parameter regimes.

In the linear regime, the edge states have been demonstrated to be topologically protected against defects in the lattice[18,20,44]. To investigate whether the edge states preserve their robustness in the nonlinear regime as well, we explore the propagation of nested solitons in the presence of a deliberately located point defect in the lattice. Specifically, we detune one of the site-ring resonators on the edge of the lattice by $20J$ (Fig. 4a) such that it is effectively decoupled from the rest of the lattice. Figure 4b–d shows the slow-time evolution of the observed single nested soliton in this lattice (Supplementary Video 3). We see that the nested soliton simply routes around the defect as it circulates along the boundary of the lattice, without losing its phase coherence. We do not observe any light pulses that are reflected from the defect or scattered into the bulk of the lattice. This clearly shows that the nested solitons are indeed topologically robust against defects in the lattice.

Discussion and outlook

The emergence of coherent temporal features, such as Turing rolls and nested solitons, and the characteristics of a nested frequency comb in the topological super-ring resonator closely resemble those of a single-ring resonator frequency comb in the regime of anomalous dispersion. This allows us to qualitatively depict the phase diagram of the topological frequency comb, as shown in Fig. 5. We perform numerical simulations at different pump powers (ε). Using spatiotemporal (fast-time) intensity distributions integrated over the edge rings (similar to Figs. 2d and 3a), we locate the regions of pump frequency detuning that lead to Turing rolls, chaos and nested solitons. In this phase diagram, we have also indicated (upper x axis) the

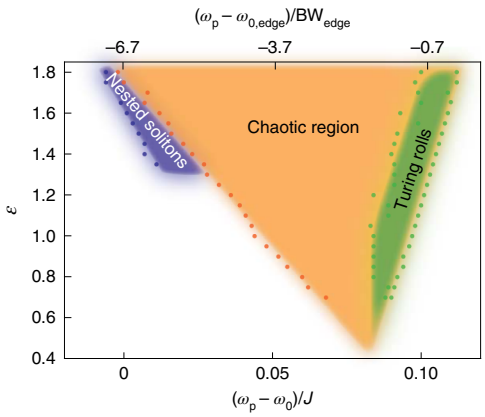

Fig. 5 | Qualitative phase diagram of the topological frequency comb. Different operating regimes of the topological comb as a function of the input pump frequency and pump power. The dots indicate the numerical simulation results.

pump frequency detuning from the respective cold-cavity (linear) edge mode resonance ($\omega_{0,edge}$) and normalized it by its bandwidth (BW_{edge}). Similar to the case of a single-ring resonator (Fig. 1d and Supplementary Fig. 2), we observe Turing rolls at low pump powers and for pump frequencies near the cold-cavity edge resonance ($\omega_{0,edge}$). In this regime, the longitudinal modes of the individual rings are phase-locked, which manifests as phase-locking of the Turing rolls across rings. However, only a single mode of the super-ring resonator is excited (Fig. 2g,i). At pump frequencies further away from the cold-cavity edge resonance, we observe a chaotic regime where multiple longitudinal modes of the super-ring resonator are excited in each longitudinal mode of the single rings. But these modes are not phase-locked. Note that in the chaotic regime, the pump frequency and intensity distribution in the lattice still correspond to those of the edge states. This clearly indicates that merely exciting the edge states of the system does not lead to self-organisation or phase-locking. The nested soliton region appears at input pump power $\varepsilon \approx 1.3$ and at pump frequencies that are far red-detuned from the cold-cavity edge resonance. In this regime, both sets of longitudinal modes (those of single rings and the super-ring) are phase-locked (Supplementary Section 6). This phase-locking is enabled by the unidirectionality and the approximately linear dispersion of the topological edge states (Supplementray Section 8). We observe that the soliton region narrows down, and it completely disappears at higher pump powers, probably leading to another chaotic regime. We note that this qualitative phase diagram was estimated for a given value of dispersion, in one of the edge mode resonances near the centre of the edge band.

While we have shown the presence of many features that are analogous to a single-ring resonator frequency comb, we have only analysed a small subset of parameters that control the topological frequency comb. Therefore, one can expect the appearance of many other known and unknown phases that can emerge from the interaction of edge and bulk modes. It would be intriguing, for example, to explore breathing Turing rolls and nested solitons, dark nested solitons, and platicons in the normal dispersion region[6,46]. In the limit of weak pump powers, our results could pave the way for the generation of quantum optical frequency combs and photonic cluster states entangled in higher dimensions using frequency–time multiplexing[49,50]. Our system could be translated to other frequency regimes of the electromagnetic spectrum, for example, to the microwave domain using circuit quantum electrodynamics platform to implement topological arrays of coupled resonators[51]. One could also explore other topological lattice models to engineer the band structure and therefore the dispersion of edge and bulk states. In fact, one could go beyond Euclidean geometries and explore the hierarchy of solitons in non-Euclidean curved space, for example, hyperbolic lattices[52]. Therefore, our results open the route to engineer nonlinear parametric processes, spontaneous formation, and self-organization of temporal solitons using synthetic magnetic fields and topological design principles.

Online content

Any methods, additional references, Nature Research reporting summaries, source data, extended data, supplementary information, acknowledgements, peer review information; details of author contributions and competing interests; and statements of data and code availability are available at https://doi.org/10.1038/s41567-021-01302-3.

Received: 4 December 2020; Accepted: 16 June 2021;
Published online: 05 August 2021

References

1. Udem, T., Holzwarth, R. & Hänsch, T. W. Optical frequency metrology. *Nature* **416**, 233–237 (2002).
2. Cundiff, S. T. & Ye, J. Colloquium: femtosecond optical frequency combs. *Rev. Mod. Phys.* **75**, 325–342 (2003).
3. Diddams, S. A., Vahala, K. & Udem, T. Optical frequency combs: coherently uniting the electromagnetic spectrum. *Science* **369**, eaay3676 (2020).
4. Kippenberg, T. J., Holzwarth, R. & Diddams, S. A. Microresonator-based optical frequency combs. *Science* **332**, 555–559 (2011).
5. Kippenberg, T. J., Gaeta, A. L., Lipson, M. & Gorodetsky, M. L. Dissipative Kerr solitons in optical microresonators. *Science* **361**, eaan8083 (2018).
6. Pasquazi, A. et al. Micro-combs: a novel generation of optical sources. *Phys. Rep.* **729**, 1–81 (2018).
7. Gaeta, A. L., Lipson, M. & Kippenberg, T. J. Photonic-chip-based frequency combs. *Nat. Photon.* **13**, 158–169 (2019).
8. Del'Haye, P. et al. Optical frequency comb generation from a monolithic microresonator. *Nature* **450**, 1214–1217 (2007).
9. Herr, T. et al. Temporal solitons in optical microresonators. *Nat. Photon.* **8**, 145–152 (2013).
10. Jang, J. K. et al. Synchronization of coupled optical microresonators. *Nat. Photon.* **12**, 688–693 (2018).
11. Tikan, A. et al. Emergent nonlinear phenomena in a driven dissipative photonic dimer. *Nat. Phys.* **17**, 1–7 (2021).
12. Helgason, Ó. B. et al. Dissipative solitons in photonic molecules. *Nat. Photon.* **15**, 305–310 (2021).
13. Vasco, J. & Savona, V. Slow-light frequency combs and dissipative Kerr solitons in coupled-cavity waveguides. *Phys. Rev. Appl.* **12**, 064065 (2019).
14. Lu, L., Joannopoulos, J. D. & Soljačić, M. Topological photonics. *Nat. Photon.* **8**, 821–829 (2014).
15. Khanikaev, A. B. & Shvets, G. Two-dimensional topological photonics. *Nat. Photon.* **11**, 763–773 (2017).
16. Ozawa, T. et al. Topological photonics. *Rev. Mod. Phys.* **91**, 015006 (2019).
17. Hafezi, M., Demler, E. A., Lukin, M. D. & Taylor, J. M. Robust optical delay lines with topological protection. *Nat. Phys.* **7**, 907–912 (2011).
18. Hafezi, M., Mittal, S., Fan, J., Migdall, A. & Taylor, J. Imaging topological edge states in silicon photonics. *Nat. Photon.* **7**, 1001–1005 (2013).
19. Rechtsman, M. C. et al. Photonic Floquet topological insulators. *Nature* **496**, 196–200 (2013).
20. Mittal, S. et al. Topologically robust transport of photons in a synthetic gauge field. *Phys. Rev. Lett.* **113**, 087403 (2014).
21. St-Jean, P. et al. Lasing in topological edge states of a one-dimensional lattice. *Nat. Photon.* **11**, 651–656 (2017).
22. Bahari, B. et al. Nonreciprocal lasing in topological cavities of arbitrary geometries. *Science* **358**, 636–640 (2017).
23. Bandres, M. A. et al. Topological insulator laser: experiments. *Science* **359**, eaar4005 (2018).
24. Yang, Z. et al. Mode-locked topological insulator laser utilizing synthetic dimensions. *Phys. Rev. X* **10**, 011059 (2020).
25. Cheng, X. et al. Robust reconfigurable electromagnetic pathways within a photonic topological insulator. *Nat. Mater.* **15**, 542–548 (2016).
26. Zhao, H. et al. Non-Hermitian topological light steering. *Science* **365**, 1163–1166 (2019).
27. Barik, S. et al. A topological quantum optics interface. *Science* **359**, 666–668 (2018).
28. Shalaev, M. I., Walasik, W., Tsukernik, A., Xu, Y. & Litchinitser, N. M. Robust topologically protected transport in photonic crystals at telecommunication wavelengths. *Nat. Nanotechnol.* **14**, 31–34 (2019).

29. Gao, X. et al. Dirac-vortex topological cavities. *Nat. Nanotechnol.* **15**, 1012–1018 (2020).
30. Lu, L., Gao, H. & Wang, Z. Topological one-way fiber of second Chern number. *Nat. Commun.* **9**, 5384 (2018).
31. Mittal, S., Goldschmidt, E. A. & Hafezi, M. A topological source of quantum light. *Nature* **561**, 502–506 (2018).
32. Mittal, S., Orre, V. V., Goldschmidt, E. A. & Hafezi, M. Tunable quantum interference using a topological source of indistinguishable photon pairs. *Nat. Photon.* **15**, 542–548 (2021).
33. Blanco-Redondo, A., Bell, B., Oren, D., Eggleton, B. J. & Segev, M. Topological protection of biphoton states. *Science* **362**, 568–571 (2018).
34. Kruk, S. et al. Nonlinear light generation in topological nanostructures. *Nat. Nanotechnol.* **14**, 126–130 (2019).
35. Smirnova, D., Leykam, D., Chong, Y. & Kivshar, Y. Nonlinear topological photonics. *Appl. Phys. Rev.* **7**, 021306 (2020).
36. Lumer, Y., Plotnik, Y., Rechtsman, M. C. & Segev, M. Self-localized states in photonic topological insulators. *Phys. Rev. Lett.* **111**, 243905 (2013).
37. Ablowitz, M. J., Curtis, C. W. & Ma, Y.-P. Linear and nonlinear traveling edge waves in optical honeycomb lattices. *Phys. Rev. A* **90**, 023813 (2014).
38. Leykam, D. & Chong, Y. D. Edge solitons in nonlinear-photonic topological insulators. *Phys. Rev. Lett.* **117**, 143901 (2016).
39. Mukherjee, S. & Rechtsman, M. C. Observation of Floquet solitons in a topological bandgap. *Science* **368**, 856–859 (2020).
40. Xue, X., Wang, P.-H., Xuan, Y., Qi, M. & Weiner, A. M. Microresonator Kerr frequency combs with high conversion efficiency. *Laser Photon. Rev.* **11**, 1600276 (2017).
41. Bao, H. et al. Laser cavity-soliton microcombs. *Nat. Photon.* **13**, 384–389 (2019).
42. Xue, X., Zheng, X. & Zhou, B. Super-efficient temporal solitons in mutually coupled optical cavities. *Nat. Photon.* **13**, 616–622 (2019).
43. Leykam, D., Mittal, S., Hafezi, M. & Chong, Y. D. Reconfigurable topological phases in next-nearest-neighbor coupled resonator lattices. *Phys. Rev. Lett.* **121**, 023901 (2018).
44. Mittal, S., Orre, V. V., Leykam, D., Chong, Y. D. & Hafezi, M. Photonic anomalous quantum Hall effect. *Phys. Rev. Lett.* **123**, 043201 (2019).
45. Chembo, Y. K. & Yu, N. Modal expansion approach to optical-frequency-comb generation with monolithic whispering-gallery-mode resonators. *Phys. Rev. A* **82**, 033801 (2010).
46. Chembo, Y. K. & Menyuk, C. R. Spatiotemporal Lugiato-Lefever formalism for Kerr-comb generation in whispering-gallery-mode resonators. *Phys. Rev. A* **87**, 053852 (2013).
47. Hansson, T., Modotto, D. & Wabnitz, S. On the numerical simulation of Kerr frequency combs using coupled mode equations. *Opt. Commun.* **312**, 134–136 (2014).
48. Godey, C., Balakireva, I. V., Coillet, A. & Chembo, Y. K. Stability analysis of the spatiotemporal Lugiato-Lefever model for Kerr optical frequency combs in the anomalous and normal dispersion regimes. *Phys. Rev. A* **89**, 063814 (2014).
49. Kues, M. et al. On-chip generation of high-dimensional entangled quantum states and their coherent control. *Nature* **546**, 622–626 (2017).
50. Reimer, C. et al. High-dimensional one-way quantum processing implemented on *d*-level cluster states. *Nat. Phys.* **15**, 148–153 (2019).
51. Carusotto, I. et al. Photonic materials in circuit quantum electrodynamics. *Nat. Phys.* **16**, 268–279 (2020).
52. Kollár, A. J., Fitzpatrick, M. & Houck, A. A. Hyperbolic lattices in circuit quantum electrodynamics. *Nature* **571**, 45–50 (2019).

Data availability

Source data are provided with this paper. All other data that support the plots within this paper and other findings of this study are available from the corresponding author upon reasonable request.

Code availability

The codes that support the findings of this study are available from the corresponding author upon reasonable request.

Acknowledgements

This research was supported by the Air Force Office of Scientific Research Multi-University Research Initiative (AFOSR-MURI grant no. FA9550-16-1-0323), Office of Naval Research Multi-University Research Initiative (ONR-MURI grant no. N00014-20-1-2325), United States Army Research Laboratory grant no. W911NF1920181 and NSF grant no. PHY1820938. Y.K.C. was supported by the Air Force Office of Scientific Research (AFOSR grant no. FA9550-20-1-0357).

Author contributions

S.M. and M.H. conceived the idea. S.M. performed the numerical simulations, analysed the data and wrote the manuscript with inputs from M.H., Y.K.C., G.M. and K.S. M.H. supervised the project.

Competing interests

S.M. and M.H. have filed a provisional patent based on the results reported in this manuscript.

Additional information

Supplementary information The online version contains supplementary material available at https://doi.org/10.1038/s41567-021-01302-3.

Correspondence and requests for materials should be addressed to S.M.

Peer review information *Nature Physics* thanks Vittorio Peano and the other, anonymous, reviewer(s) for their contribution to the peer review of this work.

Reprints and permissions information is available at www.nature.com/reprints.